

A Distributional Treatment of Real2Sim2Real for Vision-Driven Deformable Linear Object Manipulation

Georgios Kamaras^{1,2} and Subramanian Ramamoorthy^{1,3}

Abstract—We present an integrated (or end-to-end) framework for the Real2Sim2Real problem of manipulating deformable linear objects (DLOs) based on visual perception. Working with a parameterised set of DLOs, we use likelihood-free inference (LFI) to compute the posterior distributions for the physical parameters using which we can approximately simulate the behaviour of each specific DLO. We use these posteriors for domain randomisation while training, in simulation, object-specific visuomotor policies for a visuomotor DLO reaching task, using model-free reinforcement learning. We demonstrate the utility of this approach by deploying sim-trained DLO manipulation policies in the real world in a zero-shot manner, i.e. without any further fine-tuning. In this context, we evaluate the capacity of a prominent LFI method to perform fine classification over the parametric set of DLOs, using only visual and proprioceptive data obtained in a dynamic manipulation trajectory. We then study the implications of the resulting domain distributions in sim-based policy learning and real-world performance.

I. INTRODUCTION

Deformable linear object (DLO) manipulation is an active area of robotics research that deals with a variety of challenging tasks, such as needle threading, lace tying, cable rearrangement, and lasso throwing [1]–[3]. Although the geometry of a DLO is well understood, humans show dexterity in quickly estimating physical parameters, such as length and stiffness, from relatively few visual observations of object manipulation trajectories. This is often used to condition control policies within these estimations [4], [5], enabling efficient adaptive control. Achieving a similar level of robotic dexterity requires dealing with the inherent high dimensionality and nonlinearity of such tasks, challenges that are further exacerbated by the inherent noise in visual servoing [6], [7].

Learning policies in simulation and then performing a *Sim2Real* [3], [8] deployment follows the hypothesis that the numerous simulated iterations of a given task will robustify the learnt policy to parametric variations, as mentioned above [9]. However, this approach requires one to overcome the “reality gap” of robotic simulators, which is particularly problematic for soft objects.

¹Authors are with the School of Informatics, The University of Edinburgh, EH8 9AB, UK

²Corresponding author: g.kamaras-1@sms.ed.ac.uk

³s.ramamoorthy@ed.ac.uk

This work has been submitted to the IEEE for possible publication. For the purpose of open access, the authors have applied a Creative Commons Attribution (CC BY) licence to any Author Accepted Manuscript version arising from this submission.

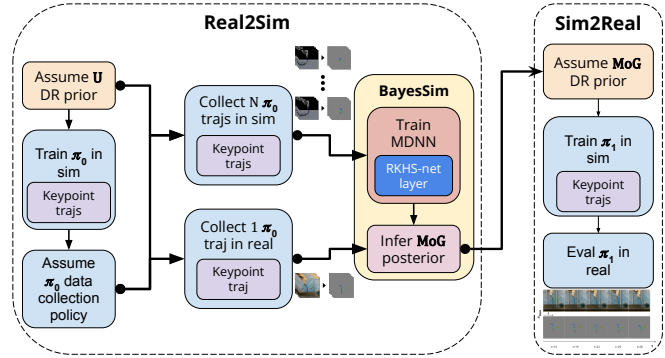


Fig. 1: Overview of our Real2Sim2Real framework. We perform inference for the posterior distribution \hat{p} over system parameters θ (Real2Sim). We use \hat{p} to perform domain randomisation while training a PPO agent to perform a visuomotor DLO control task. We deploy and evaluate our sim-trained policy in the real world (Sim2Real).

In this work, we first aim to achieve a reliable *Real2Sim* [10], [11] calibration of our simulator’s parameters θ to the real-world object parameters. Then, aiming at robust deployment, we account for any uncertainty about these parameters by exposing our learning algorithm to different hypotheses of θ .

Likelihood-free inference (LFI) deals with solving the inverse problem of probabilistically mapping real-world sensor observations to the respective simulation parameters θ that are most likely to account for the observations.

This involves inferring the multimodal distribution from which we can sample sets of simulation parameters with a high probability of replicating the modelled real-world phenomenon [12]. Any uncertainty over θ can be modelled as the variances associated with the modes.

This enables us to perform Domain Randomisation (DR), which aims to create a variety of simulated environments, each with randomised system parameters, and then to train a policy that works in all of them for a given control task objective. Assuming that the parameters of the real system is a sample in the distribution associated with the variations seen at training time, it is expected that a policy learnt in simulation under a DR regime will adapt to the dynamics of the real world environment.

Recent literature has demonstrated how distributional embeddings, such as reproducing kernel Hilbert spaces [13], of inferred keypoint trajectories combine low dimensionality and robustness to visual data noise [14], thus enabling robust Real2Sim calibration. On the Sim2Real side, we have

seen fruitful model-based Reinforcement Learning (RL) approaches [15], [16] to train deformable object manipulation policies in simulation and deploy them in the real world. However, we have yet to see an end-to-end *Real2Sim2Real* system which combines the expressiveness of Bayesian inference with the flexibility of model-free RL [17].

We propose an integrated framework addressing a number of different technical considerations (Fig. 1, Alg. 1). We use BayesSim [12] with distributional state embeddings to infer the posteriors over physical parameters θ of a set of visually observed (real) DLOs of varied length and stiffness. We use each inferred posterior $\hat{p}(\theta)$ to perform domain randomisation and train a Sim2Real transferable model-free RL policy to perform a visuomotor “reaching” task with a DLO. We deploy our sim-trained policies in the real world and compare their performance across our set of DLOs.

In this paper, we make the following contributions.

- 1) We present an **end-to-end Real2Sim2Real framework** for robust **vision-based** DLO manipulation.
- 2) We examine the capacity of BayesSim to **finely classify** the different physical properties of a deformable object drawn from a parametric set.
- 3) We study the implications of **different randomisation domains** for RL policy learning in simulation and how this translates to **real world performance**.

Our experiments show that for a parameterised set of DLOs, an integrated distributional treatment of parameter inference, policy training, and zero-shot deployment enables inferring fine differences in physical properties and adapting RL agent behaviour to them.

II. BACKGROUND

A. Likelihood-free Inference

LFI treats a simulator as a black-box generative model g with intractable likelihood, which uses its parameterisation θ to generate an output \mathbf{x} that represents the behaviour of the simulated system [18]. This process defines a likelihood function $p(\mathbf{x} | \theta)$, also called the forward model of the system, which we cannot evaluate, but we can sample from by running the simulator. To overcome the “reality gap”, we want to solve the inverse problem, which is mapping real observations \mathbf{x}^r to the parameters θ that are most likely to replicate them in simulation; let $\mathbf{x}^s = g(\theta)$. This defines the problem of approximating the posterior $\hat{p}(\theta | \mathbf{x}^s, \mathbf{x}^r)$.

BayesSim [12] approximates the posterior $\hat{p}(\theta | \mathbf{x} = \mathbf{x}^r)$ by learning the conditional density function $q_\phi(\theta | \mathbf{x})$, parameterised by ϕ . Conditional density is modelled as a mixture of Gaussians (MoG), which can be approximated by mixture density neural networks (MDNN) [19]. The inputs \mathbf{x} can be high-dimensional state-action trajectories, summary statistics $\psi(\cdot)$ of trajectory data, or kernel mappings.

BayesSim first requires training $q_\phi(\theta | \mathbf{x})$ on a dataset of N pairs (θ_n, \mathbf{x}_n) , where the parameters θ_n are drawn from a *proposal prior* $\tilde{p}(\theta)$ and the observation trajectories \mathbf{x}_n are generated by running $g(\theta_n)$ for the duration of a simulated episode and collecting the respective state-action pairs.

Then, given a single real world trajectory \mathbf{x}^r , BayesSim estimates the posterior as:

$$\hat{p}(\theta | \mathbf{x} = \mathbf{x}^r) \propto \frac{p(\theta)}{\tilde{p}(\theta)} q_\phi(\theta | \mathbf{x} = \mathbf{x}^r), \quad (1)$$

which allows the flexibility (‘likelihood-free’) for a desirable prior $p(\theta)$ which is different than the proposal prior. If $\tilde{p}(\theta) = p(\theta)$, then $\hat{p}(\theta | \mathbf{x} = \mathbf{x}^r) \propto q_\phi(\theta | \mathbf{x} = \mathbf{x}^r)$.

B. Domain Randomisation

Domain randomisation using wide uniform priors [20], combined with the inherent instability of training RL algorithms, has been shown to not provide the robustness expected in certain tasks [9], [21]. Using LFI, we obtain a posterior $\hat{p}(\theta | \mathbf{x} = \mathbf{x}^r)$ which we expect to be qualitatively more precise, i.e. narrower than the uniform prior, and more accurate, i.e. dense around the system’s true parameters.

The goal of RL is to maximise the expected sum of future discounted rewards (by γ) following a policy $\pi_\beta(\mathbf{a}_t | \mathbf{s}_t)$, parameterised by β . We formulate DR over the RL problem as maximising the joint objective:

$$\mathcal{J}(\beta) = \mathbb{E}_\theta \left[\mathbb{E}_\eta \left[\sum_{t=0}^{T-1} \gamma^t r(\mathbf{s}_t, \mathbf{a}_t) | \beta \right] \right], \quad (2)$$

where $\theta \sim \hat{p}(\theta | \mathbf{x} = \mathbf{x}^r)$ with respect to policy’s β . In the inner RL objective formulation, we follow the standard textbook denotations [22].

C. Kernel Mean Embeddings & Neural Approximation

Kernel mean embeddings map distributions into infinite-dimensional feature spaces, thus representing probability distributions without information loss to a space that enables useful mathematical operations. This happens by turning the expectation operator into a reproducing kernel Hilbert space (RKHS) inner product, which has linear complexity in the number of training points [13].

Let X be a random variable in sample space \mathcal{X} , \mathcal{F} be an RKHS with kernel $k(\mathbf{x}, \mathbf{x}')$, and data points $\mathbf{x} \in \mathcal{X}$. \mathcal{F} is a Hilbert space of functions $f : \mathcal{X} \rightarrow \mathbb{R}$ with the inner product $\langle \cdot, \cdot \rangle_{\mathcal{F}}$ [23]. Given a distribution of functions $P(X)$ and a mean embedding map $\mu_X \in \mathcal{F}$, we can recover expectations of all functions, as $\mathbb{E}_X[f(x)] = \langle \mu_X, f \rangle_{\mathcal{F}}, \forall f \in \mathcal{F}$. By Riesz representation theorem [24], μ_X exists and is unique. A common choice for the μ_X mapping is the Radial Basis Function (RBF) kernel, with parameterisable length scale σ .

Following [14], we can define the empirical kernel embedding using i.i.d. samples $\mathbf{x}_1, \dots, \mathbf{x}_N$ from $P(X)$, as:

$$\hat{\mu}_X := \frac{1}{N} \sum_{n=1}^N \phi(\mathbf{x}_n). \quad (3)$$

With *kernel trick* we avoid operating on infinite-dimensional implicit maps $\phi(\mathbf{x})$, and instead operate on a finite-dimensional Gram matrix $K: K_{ij} = k(\mathbf{x}_i, \mathbf{x}_j), i, j = 1 \dots N$ [23], which, however, is computationally expensive for large datasets ($O(n^2)$).

Following [12] (Eq. 12-15) and [14] (Eq. 6) derivations, we can use *Random Fourier Features* (RFF) [25] to approximate a shift-invariant kernel $k(\mathbf{x}, \mathbf{x}')$ by a dot product $\hat{\phi}(\mathbf{x})^T \hat{\phi}(\mathbf{x}')$, which is a more scalable approximation of K . $\hat{\phi}(\mathbf{x})$ is a finite-dimensional approximation of $\phi(\mathbf{x})$, with randomised features of the form $\langle \cos(\sigma^{-1} \circ \omega_m^T \mathbf{x}), \sin(\sigma^{-1} \circ \omega_m^T \mathbf{x}) \rangle$ (cos-sin) or $\cos(\omega_m^T \mathbf{x} + \mathbf{b}_m)$ (cos-only) [26].

Following [14], we use the RFF feature approximation to construct the kernel mean embedding of vectors (3) that can benefit from a distributional representation. This embedding approach can be integrated into a learning architecture in a fully differentiable manner, by constructing a neural network layer (RKHS-Net) that obtains random samples for frequencies ω , biases \mathbf{b} , and optionally σ (e.g., in cos-sin), and adjusts them during training by computing gradients w.r.t. the overall architecture loss.

III. METHOD

A. Keypoint detection from segmentation images

Our perception module receives an RGB image observation as input, in which it detects the environment objects of interest, i.e. the controlled DLO and the visuomotor control target. We use detection masks to create segmentation images, through which we track our task’s features for parameter inference and policy learning.

We use segmentation images to efficiently learn an unsupervised keypoint detection model, using the *transporter* method [27], as implemented by [28]. The method’s combination of keypoint-based bottleneck layer and downstream reconstruction task maintains the temporal consistency of the extracted set of keypoints. However, keypoints are inferred in every timeframe, which in practice, particularly when working with real-world image data of deformable objects, creates problems such as keypoint position noise and permutations [14].

B. Real2Sim with likelihood-free inference

Our problem is that of manipulating a DLO for a visuomotor reaching task, by learning a policy in simulation and deploying in the real-world, without any further fine-tuning. The Real2Sim part of our work deals with calibrating physical parameters that induce the deformable object’s behaviour, such as its dimensions and material behaviour, which are difficult to tune manually. Details such as camera and workspace object placement, controller stiffness parameters, etc. are beyond the scope of our work, although they can be incorporated as additional tunable parameters in extensions of our method.

For our inference and domain randomisation experiments, we define a physical parameter vector $\theta = \langle l, E \rangle$, where l denotes the length of our DLO and E denotes its Young’s modulus. Thus, we want to infer a joint posterior \hat{p} , which contains information on both the dimensions and the material properties of our deformable object. For this, we use the BayesSim-RKHS variant [14].

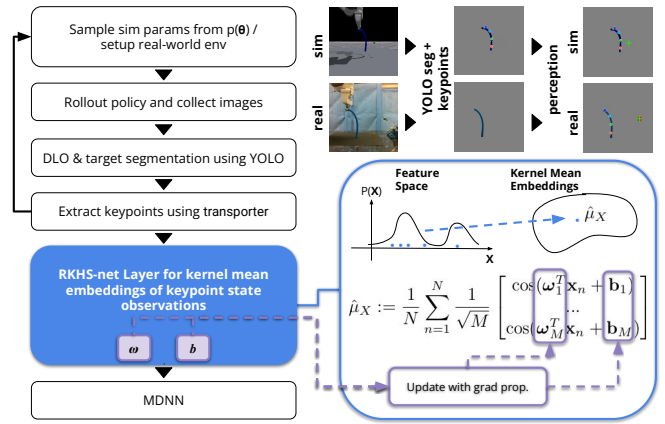


Fig. 2: An overview of our policy rollout and trajectory perception method, with keypoint extraction from segmentation images, and keypoint trajectory cos-only kernel mean embeddings using the RKHS-net layer (BayesSim-RKHS), illustration inspired by [14].

Following Algorithm 1, we begin by assuming a uniform proposal prior $\tilde{p}(\theta)$, which we use to initialise our reference prior $p_0 = \tilde{p}$. We then perform domain randomisation as $\theta \sim p_0$, while training in simulation an initial policy π_{β_0} for our task. We execute a rollout of π_{β_0} in the real world environment, to collect a real trajectory \mathbf{x}^r while manipulating a specific DLO. We perform LFI through *multiple* BayesSim iterations [14], [21]. In each inference iteration i , we use π_{β_0} as a data collection policy, running N rollouts of π_{β_0} in simulation to collect a dataset $\{(\theta, \mathbf{x}^s)\}^N, \theta \sim \tilde{p}$, which we use to train our BayesSim conditional density function q_ϕ . We use our q_ϕ and \mathbf{x}^r to compute the posterior $\hat{p}(\theta | \mathbf{x} = \mathbf{x}^r)$. We then update our reference prior $p_i = \hat{p}$ and loop again.

We can now adapt our domain randomisation distribution to the latest inferred posterior \hat{p} , and we proceed to retrain our task policy π_{β_1} . Our hypothesis is that by sampling θ from our object-specific posterior, we will get faster π_{β_1} convergence to consistently successful behaviour, and that running a rollout of π_{β_1} in the real-world environment we will collect higher cumulative reward for the specific DLO within the task episode’s horizon.

C. Keypoint trajectories in RKHS

We use an RKHS-net layer [14] to construct a distributional state representation (Fig. 2), which is provably robust to visual noise and uncertainty due to inferred keypoint permutations. Intuitively, through our kernel mean embeddings [13] we pull data from the input space (keypoint trajectory) to the feature space (RKHS). The explicit locations of the pulled points are not necessarily known or might be uncertain, but the relative similarity (inner product) of the pulled data points is known in the feature space [23]. This gives us noise robustness and permutation invariance, and it generally means that functional representations that are similar to each other are embedded closer within the RKHS, and thus they are more likely to be classified as similar.

The input of the RKHS-net layer is a vector of samples of a distribution. In this work, we compute the dis-

Algorithm 1 Real2Sim2Real for DLO manipulation

```
1: Given:  $N_{\text{LFI}}$ : inference iterations
2: Assume uniform proposal prior  $\tilde{p}(\theta) \approx U$ 
3: Assign reference prior  $p_0 \leftarrow \tilde{p}$ 
4: Train initial policy  $\pi_{\beta_0}(\mathbf{a}_t | \mathbf{s}_t)$ ,  $\theta \sim p_0$ 
5: Run 1  $\pi_{\beta_0}$  rollout in the real env to collect  $\mathbf{x}^r$ 
6: // 1. Real2Sim DLO parameter inference
7:  $i \leftarrow 0$ 
8: while  $i < N_{\text{LFI}}$  do
9:    $\{(\theta, \mathbf{x}^s)\}^N \leftarrow$  Run  $N$   $\pi_{\beta_0}$  rollouts in sim,  $\theta \sim p_i$ 
10:   Train  $q_\phi$  over  $\{(\theta, \mathbf{x}^s)\}^N$ 
11:    $\hat{p}(\theta | \mathbf{x} = \mathbf{x}^r) \propto p_i(\theta) / \tilde{p}(\theta) q_\phi(\theta | \mathbf{x} = \mathbf{x}^r)$ 
12:   Update reference prior  $p_i \leftarrow \hat{p}$ 
13:    $i \leftarrow i + 1$ 
14: end while
15: // 2. Policy training in sim
16: Train policy  $\pi_{\beta_1}(\mathbf{a}_t | \mathbf{s}_t)$ ,  $\theta \sim \hat{p}$ 
17: // 3. Sim2Real policy deployment
18: Evaluate  $\pi_{\beta_1}$  in the real env by running 1  $\pi_{\beta_1}$  rollout
```

tributional embedding for a noisy trajectory of keypoints $\mathbf{x} = (\mathbf{x}_1, \dots, \mathbf{x}_n)$, where each keypoint is defined in a 2D RGB pixel space.

D. Policy Learning and Sim2Real Deployment

We use Proximal Policy Optimisation (PPO) [17] as our reference model-free *on-policy* RL algorithm. PPO is designed to maximise the expected reward with a clipped surrogate objective to prevent large updates. It samples actions from a Gaussian distribution, which is parameterised during policy learning. We perform policy learning in simulation, performing domain randomisation using our likelihood-free inference *reference prior* p as a task parameterisation sampler, where p is either the default uniform distribution U , or an inferred MoG posterior (Alg. 1, line 12).

IV. EXPERIMENTAL SETUP

Our experiments address the following questions.

- 1) Can our inferred posteriors **describe different physical parameterisations of similarly shaped DLOs**?
- 2) What is **the impact of these posteriors on domain randomisation** using the respective MoG?
- 3) How does this impact translate into **object-centric agent performance** during real-world deployment?

A. Reference Task

To evaluate the parameter inference performance of our set-up, as well as the implications of the inferred parameter posterior $\hat{p}(\theta)$ to policy learning and deployment, we design a visuomotor task which studies the dynamic manipulation of a DLO towards a target in its workspace. Our task is inspired by established dynamic rope manipulation tasks [2], [29].

We set up our task with a robot arm that picks up the DLO from a designated position on the table \mathbf{x}_0 by grasping it near one of its tips, and raises it to a designated height h_0 . Both

\mathbf{x}_0 and h_0 , as well as our initial DLO pose, remain fixed for all of our simulation and real experiment iterations. The execution of our policy begins immediately after the object has been picked up and raised to h_0 . Thus, the dynamic nature of our task is constituted by the underactuated manner in which we control our DLO, having it dangling from one of its tips, as well as the momentum forces acting on its body ever since it was raised from the table.

The positions of both the DLO and the target are tracked in the 2D pixel space of an RGB image. More specifically, the DLO is tracked by an inferred cluster of 4 keypoints, extracted over a segmentation image, and the target with the computed pixel-space median of its own segmentation mask, which we treat as an artificial 5th keypoint. In both our parameter inference (real2sim) and policy training and deployment (sim2real) experiments, we position-control our Panda end-effector (EEF) by navigating it to a target position through inverse kinematics. Our simulator uses the IsaacGym attractors implementation, whereas in the real world we use a Cartesian impedance controller [30].

B. Simulation & Hardware setup

We setup our simulation in IsaacGym [31]. Our simulated environment contains a Franka Emika Panda 7-DoF robot arm equipped with a parallel gripper, which is on top of a tabletop workspace. On top of this workspace, a blue-coloured DLO exists, which is simulated using the corotational finite element method of the FleX physics engine. A small green spherical object is the target of our visuomotor control task. Across all our parameter inference and policy learning experiments, the simulated DLO is parameterised in the $[1e3, 5e4]$ (Pa) range for Young’s modulus and the $[195, 305]$ (mm) range for length. Thus, *median* of our simulated parameter space is $(2.55e4 \text{ Pa}, 250\text{mm})$.

Our real-world setup replicates the simulation setup as closely as possible. We extend an open-source sample-efficient robotic RL infrastructure [30] for the purpose of evaluating PPO policies [32]. For visual observations, we use a RealSense D435i camera capturing 60 fps, mounted to view our workspace from the right side. To avoid the overhead of a more elaborate sim and real camera pose calibration, we select our real-world camera placement such that the captured images qualitatively approximate the respective simulation images.

For our experiments, we manufacture 4 blue-coloured DLOs using Shore hardness 00-20 (for len. 200mm and 290mm), 00-50 (for len. 270mm) and A-40 (for len. 200mm) silicone polymers [33]. The real world green target ball is made of plasticine.

C. Perception setup

We collect visual observations using the real-time RGB image stream produced from our side-view camera. For computational efficiency, we focus our observations on our blue DLO and the green target ball using segmentation images. For this, we fine-tune the segmentation task version of YOLOv8.2 [34]. We use a dataset of 183 manually labelled

workspace images, pre-processed through auto-orientation and resizing to 256×256 , and augmented using random Gaussian blur and salt-and-pepper noise, totalling 439 images. With this dataset, we train the open source YOLO weights for another 64 epochs.

We reduce the dimensionality of our visual observations by applying a learnt model of 4 keypoints to each segmentation image in real time. We train this keypoint model using a dataset of 1500 random policy rollouts of our simulated control task, while sampling our system parameters θ from a uniform prior. In this data set, we also incorporate a small number of real-world policy rollouts, and we train for 50 epochs. These keypoints constitute our observation vector.

D. Domain Randomisation setup

In practice, we see that in popular robotics simulators, such as IsaacGym, re-parameterising an existing deformable object simulation to change physical properties such as stiffness would require to re-initialise the whole simulation. This makes it difficult to integrate such simulators in an RL environment that follows the well-established *gym* style [35].

Thus, to perform DR for our RL task, we train our policies in *vectorised* environments [32]. This enables us to launch parallel instances of our simulation, each with a different DLO parameterisation, which is sampled by our current reference prior. To further robustify the real-world performance of our sim-trained policies and minimise the need for camera calibration, we introduce a small randomness in our camera and target object poses by uniformly sampling pose offsets in the $[\pm 0.025, \pm 0.025, \pm 0.025]$ (m) and $[\pm 0.02, 0, \pm 0.02]$ (m) ranges, respectively.

We empirically select to launch 12 concurrent environments, from 12 respective domain samples, to manage our computationally intensive deformable object simulations. This places the descriptiveness of our inferred posteriors at the forefront of our experimental study, since inaccuracy and imprecision of the inferred MoGs can have worse consequences in small-data experiments. We sample our MoGs in a *low-variance* method, thus each component is likely to contribute to our set of domain samples.

E. Control setup

We command our EEF by sending it target poses (7D command vectors). For our control experiments, we constrain our EEF motion into two dimensions, moving only along the x and z axes by controlling the respective deltas. Thus, our sampled policy actions are 2D $\langle dx, dz \rangle$ vectors that we sample in the $[-0.06, 0.06]$ (m) range to maintain smooth EEF transitions. Our 12D observations are constructed by a flattened vector of the 2D desired goal, the 2D vector of the x and z components of our EEF position (proprioception) and the $4 \times 2D$ state observation, which reflects the pixel positions of our target object and DLO, respectively.

In each state s_t , we track the current distance of our DLO keypoint cluster to the desired goal, which we compute using the Frobenius norm of the respective distance matrix. Our sparse reward function uses this distance d_t and a predefined

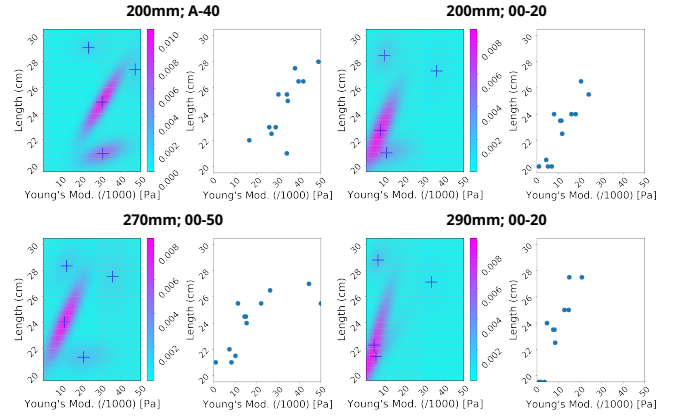


Fig. 3: Inferred MoG posterior heatmaps and the induced domain samples when each MoG is used for DR. MoG component means are displayed in blue crosses and colorbar quantifies likelihood.

pixel space distance threshold to count the reward d_{thresh} . Thus, whenever $d_t \leq d_{\text{thresh}}$, our respective reward is the distance scaled to $[0.0, 1.0]$, denoted as $r_t = 1.0 - (d_t/d_{\text{thresh}})$.

For safety reasons, we restrict our EEF motion within the $\langle x, y, z \rangle \in \langle [0.275, 0.6], [-0.1, 0.1], [0.1, 0.5] \rangle$ (m) world frame coordinates, with the base of the robot arm being on $(0, 0, 0)$. Whenever the EEF leaves this designated workspace, the episode ends as a failure with a reward of -1 .

F. Parameter Inference & Policy Algorithms training

For parameter inference, we implement the BayesSim-RKHS variant [14] (Fig. 2). Our RKHS-net layer embeds the 5 observed keypoints (4 from DLO, +1 for the desired goal) using 500 random Fourier features and cos-only components. Our MDNN models 4 mixture components with full covariance and uses 3 fully connected layers of 1024 units each. We use Adam optimiser with a learning rate of $1e-6$. As in Alg. 1, line 8, we approximate our posterior $\hat{p}(\theta)$ through 15 iterations, each increasing the training set with 100 more trajectories, whose parameters θ have been sampled using the latest posterior.

For policy learning, we use the Stable Baselines3 [32] PPO implementation. To maintain the generality of our proposed methodology, we keep the default implementation hyperparameters, which reflect the hyperparameters originally proposed in the seminal work [17]. We train for 120,000 total steps, with a maximum duration of episodes of 16 steps, and a batch size of also 16. We empirically tune our real impedance controller damping and stiffness so that 16 real-world steps approximate the respective 16 simulation steps.

V. RESULTS

A. Different Physical Parameterisations in LFI & DR

Figure 3 illustrates our Real2Sim performance using 2D MoG posterior heatmaps, along with the respective scatter plots of the 12 resulting domain samples. Each MoG has 4 components, whose mean, variance, and mixture coefficient are parameterised during inference. The tightness and spread

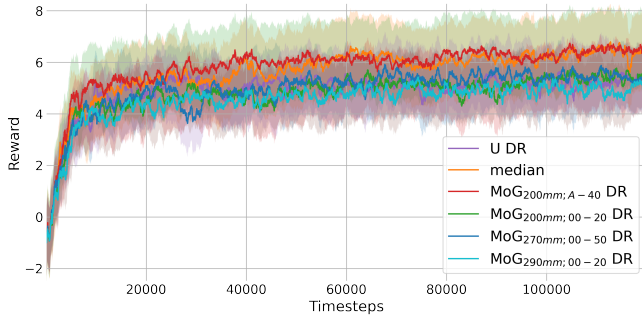


Fig. 4: Learning curves of PPO agent training when performing DR using different domain distributions.

of the posteriors serve as a qualitative indication of the precision of the inference. The crosses that represent the means of different Gaussians capture alternative hypotheses of the observed DLO’s parameterisation.

We see that for our set of DLOs, BayesSim-RKHS **correctly classifies the varied softness** (Young’s modulus); however, it **struggles to cleanly classify the varied dimension** (length). This is indicated by the MoG variance across each parameter’s axis and the respective spread of the component means, which inherently encode any uncertainty about the parameter estimation.

B. Uncertainty over Parameter Estimation & DR

Following the above property of MoG posteriors, we observe how **the relative certainty (sharpness) of a posterior** along the dimension of a variable **results in proportionately tightly clustered domain samples** along this dimension. Thus we see domain samples being mainly spread along the less certain – length – posterior dimension. This is particularly visible for the notably similar 200mm and 290mm shore 00-20 DLO posteriors.

For the 200mm; A-40 and 270mm; 00-50 DLOs, we see some *alternative hypotheses* (component means) for the DLO parameterisation that also contribute to our low-variance sampling, due to the relative magnitude of the respective mixture coefficients. This contribution is evident by the spread of the respective domain samples.

C. Object-centric Agent Performance

We train (Fig. 4) 4 PPO policies using our 4 inferred MoG posteriors (Fig. 3) for domain randomisation. We also train a policy by performing DR over a uniform distribution (PPO- U) and a policy which assumes that the simulated DLO is parameterised according to the median of our parameter space (PPO- μ). We evaluate these 6 policies in each one of our 4 real-world DLOs, repeating each evaluation 4 times for a total of 96 sim2real policy deployments. For each sim2real experiment, we compute the mean trajectories resulting from the accumulation of commanded EEF position deltas (commanded *actions*) over 4 repetitions.

These mean trajectories are presented in Fig. 5, with shaded regions showing the standard deviation between different repetitions. We observe many interesting **motion patterns, which indicate adaptation of agent performance to**

the physical parameterisation of the respective evaluation DLO. An indicative subset of these observations is extrinsically corroborated by Fig. 6. The following observations are highlighted in **olive** annotations.

We see the MoG_{200mm; A-40} policy (PPO-0, plotted on **red**) that shows the tightest “roaming pattern” (1) to maximise the stiffer and shorter 200mm; A-40 DLO reward close to the target. We also see PPO-0 following the same first half of the trajectory (2) for the softest 00-20 DLOs. Similarly, the MoG_{200mm; 00-20} policy (PPO-1, plotted on **green**), follows a very similar first third of the trajectory (3) for the softer 00-20 and 00-50 DLOs, with some material-related variance, and then attempts a similar “loop pattern” for the last 6 reaching steps with the softest 00-20 DLOs (4). In a related adaptation, we see that although both PPO-1 and MoG_{290mm; 00-20} (PPO-3, plotted on **cyan**) policies follow a similar pattern for the latter half of the trajectory for the shorter and stiffer 200mm; A-40 DLO, the PPO-1 pattern looks cleaner, due to being inherently conditioned on shorter DLOs (5).

For the MoG_{270mm; 00-50} policy (PPO-2, plotted on **blue**), we see a similar first half of the trajectory for the softer 00-20 DLOs, as well as the 270mm; 00-50 one, although with greater variance (6). We also see a similar reaching pattern in the last 6 steps for the longer 270mm and 290mm DLOs (7), with differences attributed to their different softness. PPO-2 and PPO-3 also exhibit a similar reaching pattern in the last 6 steps for the shorter and softer 200mm; 00-20 DLO (8). Finally, the most distinct sign of domain distribution adaptation occurs in PPO-3 trajectories maintaining a higher distance between the EEF and the table than any other DR policy (9).

Fig. 7 shows the space of the mean EEF trajectories (averaged over 4 repetitions) as a similarity heatmap, to give an idea of the variation in the policy space for our 6 policies evaluated over our 4 DLOs. $U, \mu, 0, 1, 2, 3$ denote the respective PPO trajectories, as indexed above. For 200mm; A-40, we see that the PPO-0 and PPO-1 trajectories, both conditioned on equally short 200mm DLO, show the greatest similarity. For 200mm; 00-20, we see that the PPO- U and PPO-2 trajectories are the most similar on average. For the longer 270mm; 00-50 and 290mm; 00-20 DLOs, we have PPO-1 and PPO-2 being the most similar on average.

VI. DISCUSSION

In this paper, we extend the Real2Sim2Real literature with a proof of concept that an integrated distributional treatment of parameter inference, policy training, and zero-shot deployment can lead to notable agent behaviour adaptation over a set of parameterised DLOs. We use a prominent LFI method (BayesSim) to capture fine parameterisation differences of similarly shaped DLOs. Using the inferred MoG posteriors for DR during RL policy training may not lead to direct benefits in training performance (although this is largely task dependent); however, we observe strong object-centric agent performance indications during real-world deployment.

This means that through an integrated distributional treatment of the Real2Sim2Real problem, practitioners of the soft

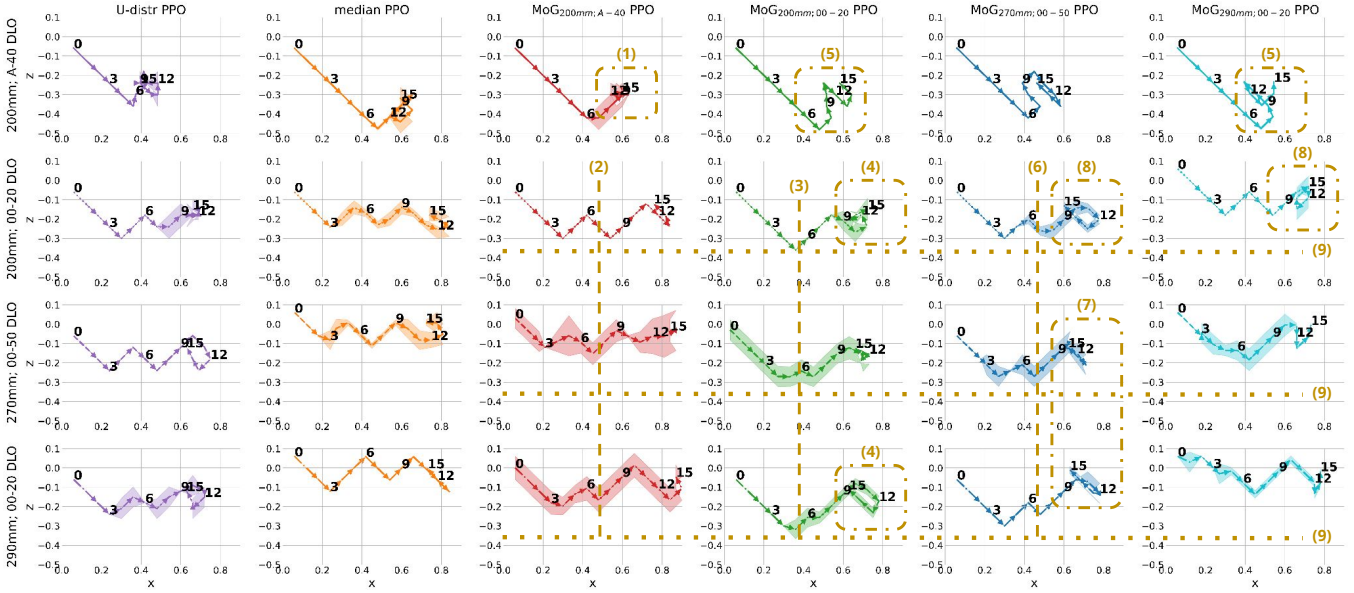


Fig. 5: EEf trajectories during the real world deployment for 4 different DLOs of 6 policies trained using different domain distributions. We repeat each deployment 4 times and average the measured accumulation of commanded EEf translations along the x and z axes (commanded *actions*), with shaded regions reporting standard deviation.

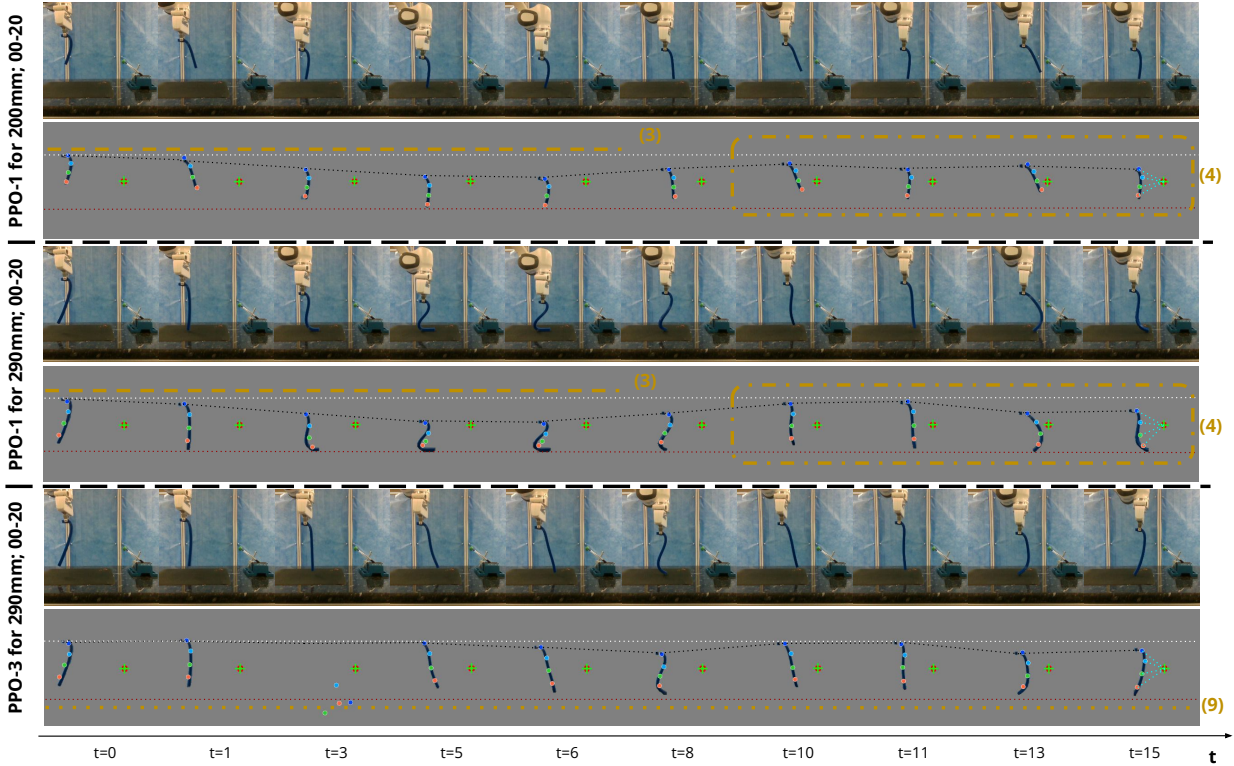


Fig. 6: Timelapses of real world MoG_{200mm; A-40} (PPO-0) policy evaluations using our 200mm; shore A-40, 270mm; shore 00-50, and 290mm; shore 00-50 DLOs, in conjunction with Figure 5. We can extrinsically confirm reported observations (3) (same 1/3 of trajectory), (4) (similar reaching pattern) and (9) (moving higher above the table).

robotics and soft body manipulation domains can condition RL policies on system parameterisations inferred through visual observations, thus inducing object-centric performance, all the while operating in a shared action and observation space for both parameter inference and policy learning. Finally, we note that our framework can be extended for dual

control by improving the posterior estimation in tandem with the task policy [21], [36].

ACKNOWLEDGMENTS

G. Kamaras is supported by the Engineering and Physical Sciences Research Council (EPSRC), as part of the CDT

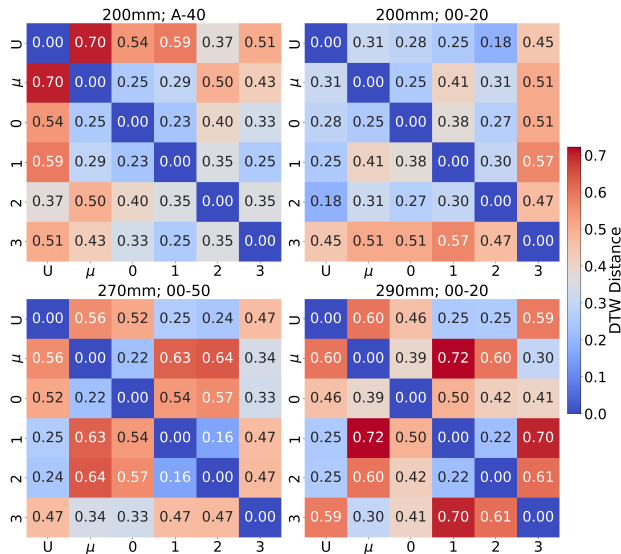


Fig. 7: Dynamic Time Wrapping (DTW) heatmap of EEF trajectories (accum. commanded actions) following trained PPO policies.

in RAS at Heriot-Watt University and The University of Edinburgh. S. Ramamoorthy is supported by a UKRI Turing AI World Leading Researcher Fellowship on AI for Person-Centred and Teachable Autonomy (grant EP/Z534833/1).

REFERENCES

- [1] H. Zhang, J. Ichnowski, D. Seita, J. Wang, H. Huang, and K. Goldberg, “Robots of the lost arc: Self-supervised learning to dynamically manipulate fixed-endpoint cables,” in *Proc. IEEE Int. Conf. Robot. and Automat.*, 2021, pp. 4560–4567.
- [2] C. Chi, B. Burchfiel, E. Cousineau, S. Feng, and S. Song, “Iterative residual policy: For goal-conditioned dynamic manipulation of deformable objects,” *Int. J. Robot. Res.*, vol. 43, no. 4, pp. 389–404, 2024.
- [3] M. Haiderbhai, R. Gondokaryono, A. Wu, and L. A. Kahrs, “Sim2real rope cutting with a surgical robot using vision-based reinforcement learning,” *IEEE Trans. Automat. Sci. Eng.*, 2024.
- [4] S. Kuroki, J. Guo, T. Matsushima, T. Okubo, M. Kobayashi, Y. Ikeda, R. Takanami, P. Yoo, Y. Matsuo, and Y. Iwasawa, “Gendom: Generalizable one-shot deformable object manipulation with parameter-aware policy,” in *Proc. IEEE Int. Conf. Robot. and Automat.*, 2024, pp. 14 792–14 799.
- [5] K. Zhang, B. Li, K. Hauser, and Y. Li, “Adaptigraph: Material-adaptive graph-based neural dynamics for robotic manipulation,” in *Robotics: Sci. Syst.*, 2024.
- [6] V. E. Arriola-Rios, P. Guler, F. Ficuciello, D. Kragic, B. Siciliano, and J. L. Wyatt, “Modeling of deformable objects for robotic manipulation: A tutorial and review,” *Front. Robot. AI*, p. 82, 2020.
- [7] H. Yin, A. Varava, and D. Kragic, “Modeling, learning, perception, and control methods for deformable object manipulation,” *Sci. Robot.*, vol. 6, no. 54, 2021, Art. no. eabd8803.
- [8] X. Liang, F. Liu, Y. Zhang, Y. Li, S. Lin, and M. Yip, “Real-to-sim deformable object manipulation: Optimizing physics models with residual mappings for robotic surgery,” in *Proc. IEEE Int. Conf. Robot. and Automat.*, 2024, pp. 15 471–15 477.
- [9] X. B. Peng, M. Andrychowicz, W. Zaremba, and P. Abbeel, “Sim-to-real transfer of robotic control with dynamics randomization,” in *Proc. IEEE Int. Conf. Robot. and Automat.*, 2018, pp. 3803–3810.
- [10] B. Mehta, A. Handa, D. Fox, and F. Ramos, “A user’s guide to calibrating robotic simulators,” in *Proc. Conf. Robot Learn.*, 2021, pp. 1326–1340.
- [11] J. Liang, S. Saxena, and O. Kroemer, “Learning active task-oriented exploration policies for bridging the sim-to-real gap,” in *Robotics: Sci. Syst.*, 2020.
- [12] F. Ramos, R. C. Possas, and D. Fox, “Bayessim: adaptive domain randomization via probabilistic inference for robotics simulators,” in *Robotics: Sci. Syst.*, 2019.
- [13] K. Muandet, K. Fukumizu, B. Sriperumbudur, B. Schölkopf, *et al.*, “Kernel mean embedding of distributions: A review and beyond,” *Found. Trends Mach. Learn.*, vol. 10, no. 1-2, pp. 1–141, 2017.
- [14] R. Antonova, J. Yang, P. Sundaresan, D. Fox, F. Ramos, and J. Bohg, “A bayesian treatment of real-to-sim for deformable object manipulation,” *IEEE Robot. Automat. Lett.*, vol. 7, no. 3, pp. 5819–5826, 2022.
- [15] A. Zeng, P. Florence, J. Tompson, S. Welker, J. Chien, M. Attarian, T. Armstrong, I. Krasin, D. Duong, V. Sindhwani, *et al.*, “Transporter networks: Rearranging the visual world for robotic manipulation,” in *Proc. Conf. Robot Learn.*, 2021, pp. 726–747.
- [16] D. Seita, P. Florence, J. Tompson, E. Coumans, V. Sindhwani, K. Goldberg, and A. Zeng, “Learning to rearrange deformable cables, fabrics, and bags with goal-conditioned transporter networks,” in *Proc. IEEE Int. Conf. Robot. and Automat.*, 2021, pp. 4568–4575.
- [17] J. Schulman, F. Wolski, P. Dhariwal, A. Radford, and O. Klimov, “Proximal policy optimization algorithms,” *arXiv preprint arXiv:1707.06347*, 2017.
- [18] G. Papamakarios and I. Murray, “Fast ϵ -free inference of simulation models with bayesian conditional density estimation,” *Adv. Neural Inf. Process. Syst.*, vol. 29, 2016.
- [19] C. M. Bishop, *Mixture density networks*. Aston University, 1994.
- [20] J. Tobin, R. Fong, A. Ray, J. Schneider, W. Zaremba, and P. Abbeel, “Domain randomization for transferring deep neural networks from simulation to the real world,” in *Proc. IEEE/RSJ Int. Conf. Intell. Robots Syst.*, 2017, pp. 23–30.
- [21] R. Possas, L. Barcelos, R. Oliveira, D. Fox, and F. Ramos, “Online bayessim for combined simulator parameter inference and policy improvement,” in *Proc. IEEE/RSJ Int. Conf. Intell. Robots Syst.*, 2020, pp. 5445–5452.
- [22] R. S. Sutton, *Reinforcement learning: An introduction*. A Bradford Book, 2018.
- [23] B. Ghojogh, A. Ghodsi, F. Karray, and M. Crowley, “Reproducing Kernel Hilbert space, Mercer’s Theorem, Eigenfunctions, Nyström Method, and Use of Kernels in Machine Learning: Tutorial and Survey,” *arXiv preprint arXiv:2106.08443*, 2021.
- [24] N. I. Akhiezer and I. M. Glazman, *Theory of linear operators in Hilbert space*. Courier Corporation, 2013.
- [25] A. Rahimi and B. Recht, “Random features for large-scale kernel machines,” *Adv. Neural Inf. Process. Syst.*, vol. 20, 2007.
- [26] F. T. Ramos, R. Antonova, A. Handa, and D. Fox, “Method to incorporate uncertain inputs into neural networks,” June 1 2023, uS Patent App. 17/540,107.
- [27] T. D. Kulkarni, A. Gupta, C. Ionescu, S. Borgeaud, M. Reynolds, A. Zisserman, and V. Mnih, “Unsupervised learning of object keypoints for perception and control,” *Adv. Neural Inf. Process. Syst.*, vol. 32, 2019.
- [28] Y. Li, A. Torralba, A. Anandkumar, D. Fox, and A. Garg, “Causal discovery in physical systems from videos,” *Adv. Neural Inf. Process. Syst.*, vol. 33, 2020.
- [29] V. Lim, H. Huang, L. Y. Chen, J. Wang, J. Ichnowski, D. Seita, M. Laskey, and K. Goldberg, “Real2sim2real: Self-supervised learning of physical single-step dynamic actions for planar robot casting,” in *Proc. IEEE Int. Conf. Robot. and Automat.*, 2022, pp. 8282–8289.
- [30] J. Luo, Z. Hu, C. Xu, Y. L. Tan, J. Berg, A. Sharma, S. Schaal, C. Finn, A. Gupta, and S. Levine, “Serl: A software suite for sample-efficient robotic reinforcement learning,” in *Proc. IEEE Int. Conf. Robot. and Automat.*, 2024, pp. 16 961–16 969.
- [31] V. Makoviychuk, L. Wawrzyniak, Y. Guo, M. Lu, K. Storey, M. Macklin, D. Hoeller, N. Rudin, A. Allshire, A. Handa, and G. State, “Isaac gym: High performance gpu-based physics simulation for robot learning,” 2021.
- [32] A. Raffin, A. Hill, A. Gleave, A. Kanervisto, M. Ernestus, and N. Dormann, “Stable-baselines3: Reliable reinforcement learning implementations,” *J. Mach. Learn. Res.*, vol. 22, no. 268, pp. 1–8, 2021.
- [33] Z. Liao, M. Hossain, and X. Yao, “Ecoflex polymer of different shore hardnesses: Experimental investigations and constitutive modelling,” *Mech. Mater.*, vol. 144, p. 103366, 2020.
- [34] J. Redmon, S. Divvala, R. Girshick, and A. Farhadi, “You only look once: Unified, real-time object detection,” in *Proc. IEEE Conf. Comput. Vis. Pattern Recognit.*, 2016, pp. 779–788.
- [35] M. Towers, A. Kwiatkowski, J. Terry, J. U. Balis, G. De Cola, T. Deleu, M. Goulão, A. Kallinteris, M. Krimmel, A. KG, *et al.*, “Gymnasium: A standard interface for reinforcement learning environments,” *arXiv preprint arXiv:2407.17032*, 2024.
- [36] L. Barcelos, R. Oliveira, R. Possas, L. Ott, and F. Ramos, “Disco: double likelihood-free inference stochastic control,” in *Proc. IEEE Int. Conf. Robot. and Automat.*, 2020, pp. 10 969–10 975.